



**HAL**  
open science

# Thomson scattering investigations of a low-power Hall thruster in standard and magnetically-shielded configurations

Benjamin Vincent, Sedina Tsikata, Stéphane Mazouffre, Claude Boniface

► **To cite this version:**

Benjamin Vincent, Sedina Tsikata, Stéphane Mazouffre, Claude Boniface. Thomson scattering investigations of a low-power Hall thruster in standard and magnetically-shielded configurations. 36th International Electric Propulsion Conference, Sep 2019, Vienne, Austria. hal-02346188

**HAL Id: hal-02346188**

**<https://hal.science/hal-02346188>**

Submitted on 4 Nov 2019

**HAL** is a multi-disciplinary open access archive for the deposit and dissemination of scientific research documents, whether they are published or not. The documents may come from teaching and research institutions in France or abroad, or from public or private research centers.

L'archive ouverte pluridisciplinaire **HAL**, est destinée au dépôt et à la diffusion de documents scientifiques de niveau recherche, publiés ou non, émanant des établissements d'enseignement et de recherche français ou étrangers, des laboratoires publics ou privés.

# Thomson scattering investigations of a low-power Hall thruster in standard and magnetically-shielded configurations

IEPC-2019-384

*Presented at the 36th International Electric Propulsion Conference  
University of Vienna, Austria  
September 15-20, 2019*

B. Vincent\* S. Tsikata<sup>†</sup> and S. Mazouffre<sup>‡</sup>

*ICARE, CNRS (UPR 3021), 1C Avenue de la Recherche Scientifique, 45071 Orleans Cedex 2, France*

C. Boniface<sup>§</sup>

*CNES, 18 Avenue Edouard Belin, 31401 Toulouse Cedex 9, France*

Reliable measurements of electron properties are key for the validation of simulations of Hall thrusters and similar plasma sources. In this paper, a recently-developed incoherent Thomson scattering diagnostic is successfully applied to electron property measurement in a low-power Hall thruster discharge. Investigations on both conventional and magnetically-shielded architectures of electron properties along radial and azimuthal directions are performed. The high diagnostic sensitivity gives access to electron property measurements in a plasma environment with densities as low as  $10^{16} \text{ m}^{-3}$ . Electron temperatures reaching several tens of eV and drift velocities on the order of  $10^6 \text{ m s}^{-1}$  are measured in the exit plane region. Axial distance and discharge voltages explorations were realized. Thomson spectrum distributions characteristic of electrons out of thermal equilibrium were observed at low discharge voltage and close from the exit plane, the derived EEDF suggests the presence of a second electron population around 100 eV.

## Nomenclature

$n_e$	= electron density
$T_e$	= electron temperature
$v_{e,drift}$	= electron drift velocity
$E$	= electron energy
$\vec{k}_i$	= incident wave-vector
$\vec{k}_s$	= scattering wave-vector
$\vec{k}$	= probed wave-vector
$\theta$	= scattering angle (between $\vec{k}_i$ and $\vec{k}_s$ )
$c_1$	= coefficient for calibration of the transmission efficiency of the detection branch
$I_i$	= power of the laser light inside the observation volume
$L$	= Length of the observation volume
$\delta\lambda$	= spectral width associated to one pixel
$d\sigma_T/d\Omega$	= differential cross section for Thomson scattering

---

\*PhD student, ICARE, CNRS (UPR 3021), benjamin.vincent@cnrs-orleans.fr 

<sup>†</sup>Researcher, ICARE, CNRS (UPR 3021), sedina.tsikata@cnrs-orleans.fr 

<sup>‡</sup>Director of research, ICARE, CNRS (UPR 3021), stephane.mazouffre@cnrs-orleans.fr 

<sup>§</sup>Dr, Electric propulsion engineer, Propulsion Pyrotechnics and Aerothermodynamics service, CNES, claude.boniface@cnes.fr

$\Delta\lambda_g$	= standard deviation of the Gaussian distribution used for fitting
$\lambda_0$	= mean of the Gaussian distribution used for fitting
$\vec{E}$	= electric field
$\vec{B}$	= magnetic field
$m_i$	= mass of an ion
$v_i$	= axial velocity of an ion
$q$	= charge state of an ion
$U_d$	= discharge voltage
$T_d$	= discharge current
$\eta_{prop}$	= propellant utilization efficiency
$\dot{m}_n$	= propellant/neutrals mass flow through the anode
$I_T(\lambda)$	= signal measurement from Thomson scattering
$S_T(n_e, \Delta\lambda_g, \lambda_0, \lambda)$	= function used to fit the Thomson spectrum under the hypothesis of thermal equilibrium
$f_E(E)$	= electron energy distribution function

## I. Introduction

A Hall thruster is an electric propulsion device first conceived and developed in the mid-1960s in the Soviet Union. This thruster was operated for the first time in space aboard the USSR Meteor satellite in 1972<sup>1-4</sup> and is today widely used for station-keeping on telecommunications satellites. In spite of the long flight heritage of these devices, an understanding of their underlying physics remains poor. Aspects such as multi-scale instabilities,<sup>5</sup> non-Maxwellian electron velocity distribution functions<sup>6,7</sup> and plasma-wall interaction through secondary electron emission<sup>8-10</sup> contribute to the complexity of Hall thruster physics. To date, simulations which can capture all aspects of such physics are lacking, though development efforts are underway in several research teams. These codes must be validated through comparison with accurate experimental measurements.

Electron property measurement in Hall thrusters has so far been performed with Langmuir probes by several authors in Refs. 11–14, and by optical emission spectroscopy in Refs. 15–18. Such techniques are adequate for far plume measurements, however, their application in the acceleration region of the Hall thruster plasma has limitations.<sup>19</sup> The expected high electron densities and temperatures and the presence of strong magnetic fields in this region complicate signal measurement and interpretation.

Thomson scattering applied to such measurements offers the possibility of unambiguous and perturbation-free measurement of electron properties. The challenge associated with this technique is achieving a high enough diagnostic sensitivity for measurements in a low-density plasma, such as that of the Hall thruster. In the coherent regime, Thomson scattering has already proven to be an efficient technique to measure electron density fluctuations in such plasmas, seen in the implementation of the PRAXIS diagnostic.<sup>20</sup> In the incoherent regime, Thomson scattering allows electron temperature and density measurement.

Recent studies by Washeleski<sup>21,22</sup> have shown that this technique can be used in Hall thrusters, but the low signal levels and large stray light intensities make its application challenging. In our previous work, a sufficiently sensitive diagnostic named THETIS (*THomson scattering Experiments for low-Temperature Ion Sources*) was developed and successfully tested on a cathode discharge<sup>23</sup> and a planar magnetron.<sup>24</sup> In this paper, the results from the implementation of this diagnostic on a low-power Hall thruster are presented.

In Section II, a description of the main features of the diagnostic and the data analysis procedures used are presented. Results of experimental investigations on two thruster architectures under different discharge conditions are discussed in Section III. A summary of the main results is given in Section IV.

## II. Experimental schemes

### A. Overview of the experimental set-up

#### 1. Test facility

Experiments were performed in the NExET (*New Experiments in Electric Thrusters*) vacuum chamber at ICARE. This chamber is a stainless steel cylinder 0.7 m in diameter and 1.7 m in length, equipped with a primary dry pump, turbomolecular pump, and cryogenic pump. The pumping assembly achieves a base pressure of  $10^{-4}$  Pa and operating pressure below  $2 \times 10^{-2}$  Pa with a xenon mass flow rate up to  $2.5 \text{ mg s}^{-1}$ . The discharge voltage is regulated with an SM1500 Delta Elektronika DC power supply. Discharge current is measured through a 0.5–1.0 W Stangenes current transformer probe and monitored with a LeCroy HDO6104 digital oscilloscope.

#### 2. Plasma sources

Incoherent Thomson Scattering (ITS) measurements were performed on two 200 W Hall thrusters of the ISCT200 (*ICARE Small Customizable Thruster 200W*) type: the ISCT200-GEO and ISCT200-MS. Both thrusters were equipped with BNSiO<sub>2</sub> channels and have the same channel width and mean diameter, a geometry referred as “2S<sub>0</sub>” in previous publications.<sup>25</sup> The so-called 2S<sub>0</sub> geometry corresponds to a configuration with a channel width to diameter ratio twice as large as the usual value. In this paper, thrusters were operated with a xenon flow injected upstream of the anode.

The ISCT200-GEO has been extensively studied at the ICARE laboratory.<sup>26</sup> It has a standard magnetic field topology, achieved using an assembly of permanent magnets, with the maximum field intensity at the center of the channel and inside the exit plane. The magnetic field intensity is changed by varying the number of magnets of the internal and external magnetic circuits. Three peak magnetic fields were used:

$B_{low}$  (15 mT),  $B_{mid}$  (25 mT) and  $B_{high}$  (31.5 mT). The ISCT200-GEO is shown in Fig. 1a. The typical magnetic profile of this thruster is illustrated in the upper half of Fig. 2.

The ISCT200-MS has been studied in recent years<sup>27,28</sup> and has a magnetic circuit designed for “magnetic shielding”, a concept originally developed by researchers at NASA-JPL<sup>29</sup> and recently extended to miniature Hall thrusters (in the 300–500 W range) by Conversano and colleagues.<sup>30</sup> This configuration is designed to reduce channel erosion<sup>31</sup> and the maximum magnetic field position is slightly shifted downstream of the exit plane. This thruster were design for a nominal peak magnetic field of 15 mT ( $B_{low}$ ). For this reason, only the results obtained with the ISCT200-GEO in the  $B_{low}$  configuration will be presented for comparison between the two thrusters. The ISCT200-MS is shown in Fig. 1b and the typical magnetic field line shape of this shielded thruster is illustrated in the lower half of Fig. 2.

Both thrusters were operated with a 5 A MIREA-type hollow cathode equipped with a LaB<sub>6</sub> emissive element heated with 130 W of power and run with a xenon flow rate of 0.2 mg s<sup>-1</sup>.

The laser beam used to probe the plasma was kept fixed. The thrusters were translated along the x-axis (Fig. 3) for axial exploration of electron properties. Displacements along the y-axis and z-axis were used to change the scattering configuration.

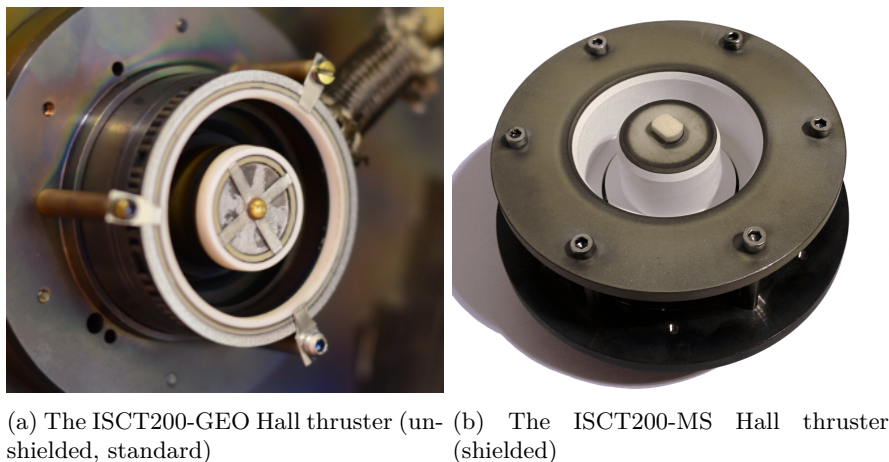


Figure 1: Hall thruster models used for ITS investigations

## B. Overview of the ITS diagnostic

A detailed description of the recently-developed ITS diagnostic named THETIS and the procedure for data analysis can be found in a published article.<sup>23</sup> Only a brief description is made here.

### 1. Optical elements

A schematic of the THETIS diagnostic transmission and detection branches is shown in Fig. 3.

The transmission branch produces the scattering signal. This is drawn with a dark green line in Fig. 3. It starts with a frequency-doubled, 10 Hz pulsed Q-switch Nd:YAG laser delivering pulses of 430 mJ (pulse width 6 ns). Mirrors and lenses conduct and focus the laser beam into the observation volume of the detection branch. The laser beam is finally sent to a large-aperture beam dump to reduce back reflections.

The detection branch is used to analyze the Thomson scattering signal and is indicated with a light green line in Fig. 3. It starts at the observation volume position, where the light from the transmission branch has been focused. From this volume, the Thomson scattering radiation and other stray radiation is emitted. This signal is focused with a collection lens onto the entrance of an optical fiber bundle, composed of a 5 × 3 array of 300 μm-diameter fibers. In the configuration of these experiments, the collection lens referred as L1 is a 100 mm-diameter plano-convex lens with a 200 mm focal length positioned at the top of the vacuum chamber 0.564 m from the observation volume (magnification factor of 0.55). The fiber bundle transmits the collected light to the optical table, where light from a 1 × 15 array of the fiber stack is collimated with a 50 mm-diameter plano-convex lens of 125 mm focal length. The stray light from reflections and Rayleigh scattering are then attenuated with a 25 mm × 25 mm VBG-NF (Volume Bragg Grating Notch Filter). The remaining

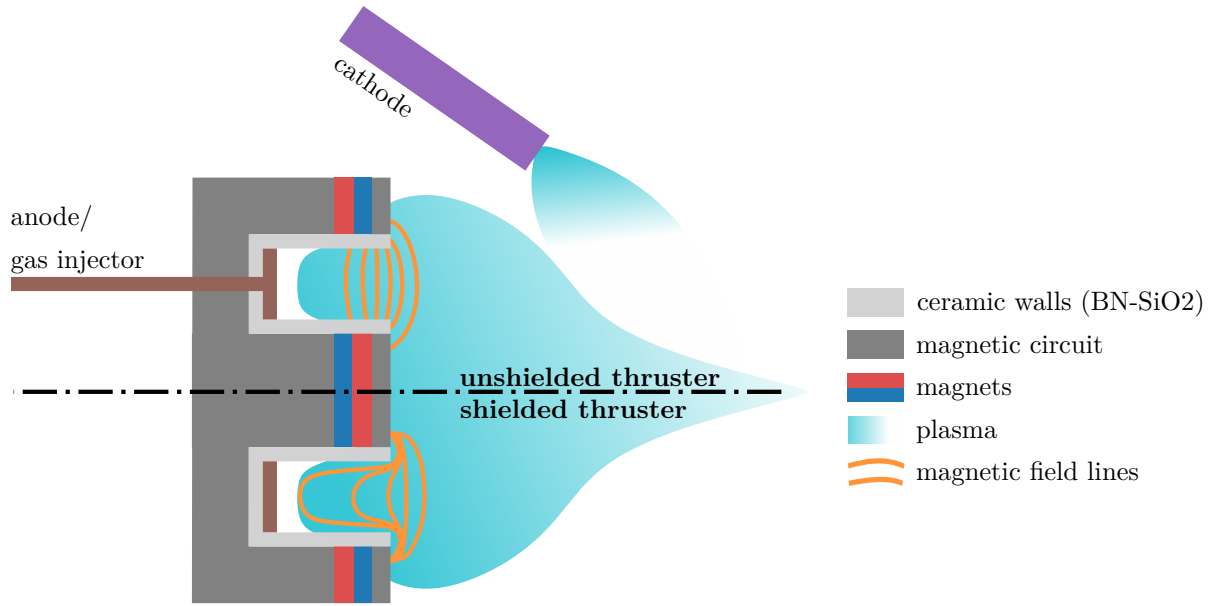


Figure 2: Hall thruster geometry. Typical magnetic field line shapes for unshielded (top half) and shielded (bottom half) Hall thrusters are compared.

light is focused onto the 1 mm-wide entrance slit of a spectrometer using a 300 mm focal length lens to fit the  $f/9.7$  numerical aperture of the spectrometer. Light is then typically dispersed by the spectrometer with a  $600 \text{ lines mm}^{-1}$  grating suited for measurement of the high electron temperatures (tens of eV) expected at the Hall thruster exit plane. Finally, the dispersed light is detected with an ICCD camera with a 10 ns gate, synchronized with the Q-switch signal from the laser.

## 2. Scattering configuration

With this detection branch configuration, the observation volume is 0.3 mm in diameter and 2.7 mm in length. Plasma properties measured with the diagnostic correspond to an average over this volume.

Electron properties along an observation wave vector  $\vec{k}$  are probed with Thomson scattering diagnostics. As represented in Fig. 4, the observation wave vector direction in this work is defined by the vector equation  $\vec{k} = \vec{k}_i - \vec{k}_s$ .  $\vec{k}_i$  corresponds to the wave vector of the incident laser beam and  $\vec{k}_s$  corresponds to the wave vector of the light entering the detection branch.

In these experiments, the thruster vertical position was chosen so that the laser beam passes at a height  $r_{mean} \times \cos(45^\circ)$  above the midplane (where  $r_{mean}$  is the mean channel diameter). With this configuration, a lateral translation of the thruster allows the alignment of the observation wave vector along either the radial or azimuthal direction, if the observation volume is positioned in front of the channel mean diameter.

By convention, a positive spectral shift of the Thomson spectrum corresponds to a positive electron drift velocity. With the data analysis convention used, a positive drift velocity measured along the azimuthal direction corresponds to electrons drifting in the anti-clockwise direction (i.e. along  $\vec{k}$ ). Along the radial direction, a positive drift will correspond to an electron moving towards the internal pole of the thruster.

## 3. Data analysis for thermal properties estimation

For calibration of the transmission factor of the detection branch, the same procedure as that discussed in Ref. 23 is followed. The vacuum chamber was filled with nitrogen to a pressure of 1000 Pa and the signal from Raman scattering accumulated over 6000 laser pulses. Due to the high electron temperatures expected with the Hall thruster, most of Thomson spectrum acquisitions were performed with the  $600 \text{ lines mm}^{-1}$  grating and a central wavelength of 532 nm. However, the Raman calibration was performed with both the  $600 \text{ lines mm}^{-1}$  and  $2400 \text{ lines mm}^{-1}$  in order to estimate the variation of the transmission efficiency of the

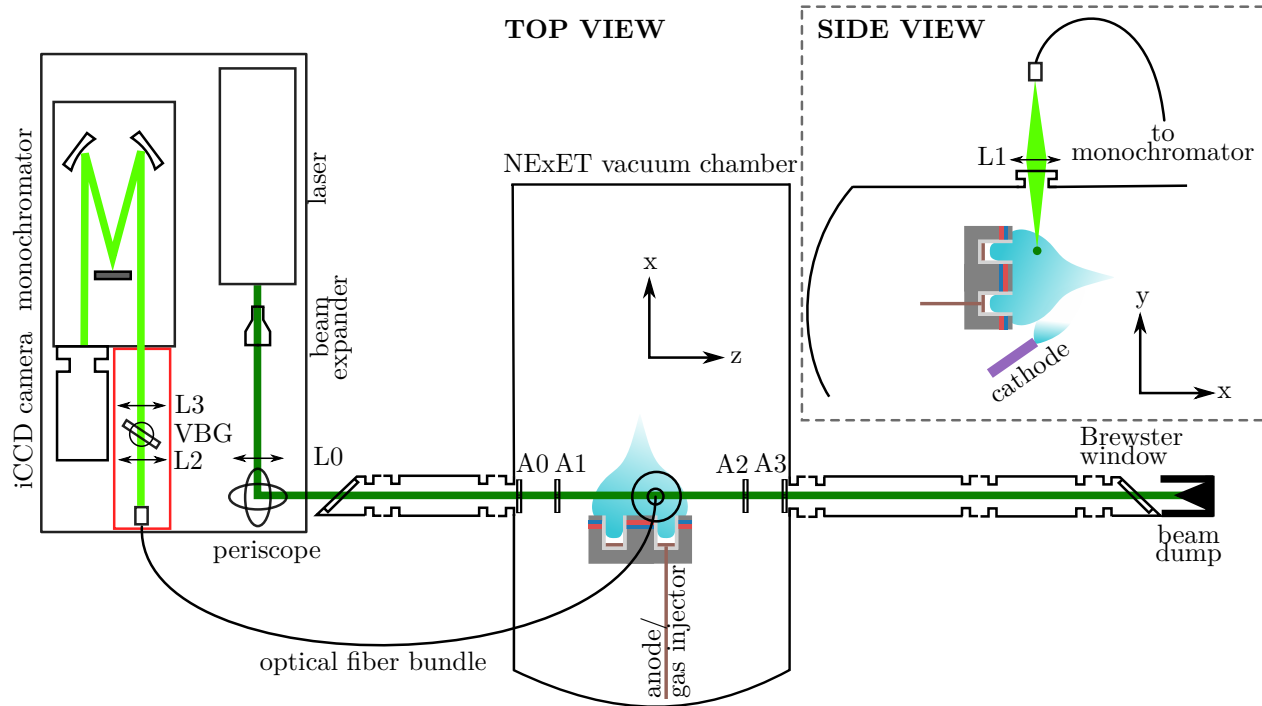


Figure 3: Schematic view of the THETIS diagnostic setup for Hall thruster investigations (not to scale). The transmission branch is indicated with a dark green line and the detection branch with a light green line. L0, L1, L2, and L3 indicate lenses; A0, A1, A2, and A3 indicate apertures; VBG indicates the notch filter. The plasma volume is shown in blue.

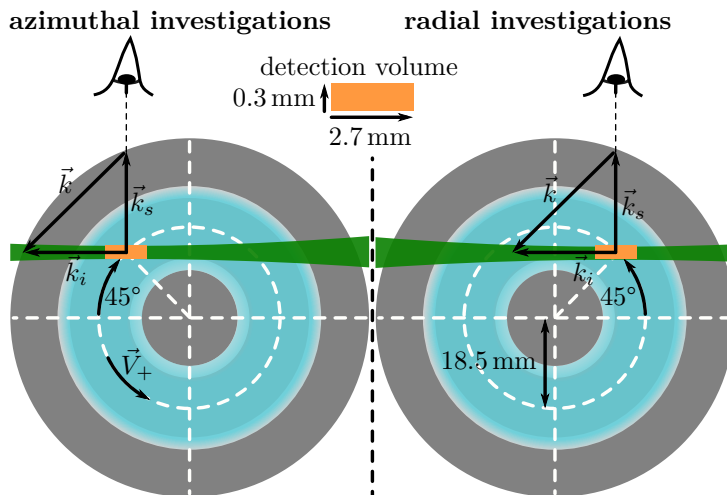


Figure 4: Scattering configurations (not to scale) used for investigation of electron properties along with the azimuthal (left) and radial (right) directions. Both views are presented facing the thruster plume (in blue). The laser beam is in green and the detection volume in orange.

detection branch with the more dispersive grating. The spectrometer slit width was set to 1 mm. With this grating and slit width the Boltzmann distribution of the vibrational states, and not the individual Raman lines, is resolved.

In our recent work, the Thomson scattering signal analyzed is obtained from the subtraction of two consecutive spectra types accumulated over 6000 laser pulses. The first record (“Thomson”), is obtained with the plasma and laser on. During this record, the Thomson scattering, plasma emission, electronic noise and the remaining stray light from Rayleigh and reflections are measured. The second record, (“background”), is obtained with the plasma on but the laser off. During this record, only the plasma emission and electronic noise signals are measured. For both plasma sources studied to date (the hollow cathode and planar magnetron) the subtraction of these two records were enough to isolate Thomson scattering from plasma emission lines.

For analysis of the Thomson spectra in the present work, the data analysis procedure has been modified with respect to the procedure described in Ref. 23 to be more robust to potential distortion from plasma emission lines. Due to the high electron temperatures, the spectral range covered by the Thomson scattering signal is large. Inside the 28.6 nm spectral range observed, several intense emission lines from the Hall thruster plasma are present. Even during the 10 ns observation gate of the detector, some emission lines remain at amplitudes at least one order of magnitude above the maximum Thomson scattering signal. The subtraction of the plasma emission record can lead to some residual distortion of the Thomson spectrum, an example of which is shown in Fig. 5. The presence of residual plasma emission can be accounted for in two ways.

A slow drift in the plasma conditions due to thermalization of the thruster could lead to a drift of plasma emission intensity. This slight difference occurring between the “Thomson” and “background” records would appear significant in comparison to the weak Thomson scattering signal. Another possible reason is that during “Thomson” records, the emission lines are measured in the presence of the intense electric field of the laser. This electric field may induce significant Stark splitting and shifting<sup>32,33</sup>. During the “background” records such splitting is absent, the recorded emission lines would not be identical to those obtained during “Thomson” records.

To limit distortion by the emission lines, the Thomson spectra are analyzed in the following way before fitting. Negative values of intensity (counts) below three times the standard deviation of the electronic noise level from the iCCD ( $\sigma_{elec\ noise}$ ) can only be attributed to distortion from plasma emission lines following subtraction. Intensities of the acquired Thomson spectra below this critical value were truncated at this value ( $3 \times \sigma_{elec\ noise} = -2.5$  counts with the experimental parameters used during the campaign). To mitigate the positive distortion of the Thomson spectrum (i.e., cases where the residual emission lines add up positively to the Thomson signal), a Savitzky–Golay filter was applied to the Thomson spectrum. This low-pass filter reduces the fast rises of intensity due to plasma emission lines, while leaving unchanged the slowly-varying Thomson spectral shape. This filter was applied independently on the left and right sides of the Thomson spectrum, separated by the rejected central spectral range around 532 nm.

Data obtained from this preliminary data processing is used as input to the algorithm for Thomson spectral analysis presented in Ref. 23. A Gaussian function convoluted with the instrument function ( $f(\lambda)$ ) is used as a fitting function for the Thomson spectrum, it can be expressed as

$$S_T(n_e, \Delta\lambda_g, \lambda_0, \lambda) = n_e c_1 I_i L \delta\lambda \frac{d\sigma_T}{d\Omega}(\vec{e}_{s,\perp}) \int_{-\infty}^{+\infty} \frac{1}{\Delta\lambda_g} \exp\left(-\frac{(u - \lambda_0)^2}{2\Delta\lambda_g^2}\right) f(\lambda - u) du \quad (1)$$

With  $c_1$  a calibration coefficient obtained from Raman scattering,  $I_i$  the incident laser intensity,  $L$  the length of the scattering volume,  $\delta\lambda$  the spectral width associated to one pixel and  $\frac{d\sigma_T}{d\Omega}(\vec{e}_{s,\perp})$  the differential cross-section for Thomson scattering along the probe wave-vector.

After the Raman calibration, the electron density average over the observation volume is directly extracted as an output parameter of the Thomson spectrum fit. The Gaussian standard deviation ( $\Delta\lambda_g$ ) and the shift of its mean ( $\lambda_0$ ) from the laser wavelength ( $\lambda_i$ ) are used to estimated the electron temperature and drift velocity with the following formulas

$$\begin{cases} T_e = \frac{m_e c^2}{4k_B} \left( \frac{\Delta\lambda_g}{\lambda_i \sin(\theta/2)} \right)^2 \\ v_{e,drift} = c \frac{\lambda_0 - \lambda_i}{2\lambda_i \sin(\theta/2)} \end{cases} \quad (2)$$

With  $m_e$  the electron mass,  $c$  the light speed in vacuum and  $\theta$  the scattering angle between the incident wave-vector ( $\vec{k}_i$ ) and the scattering wave-vector ( $\vec{k}_s$ ).

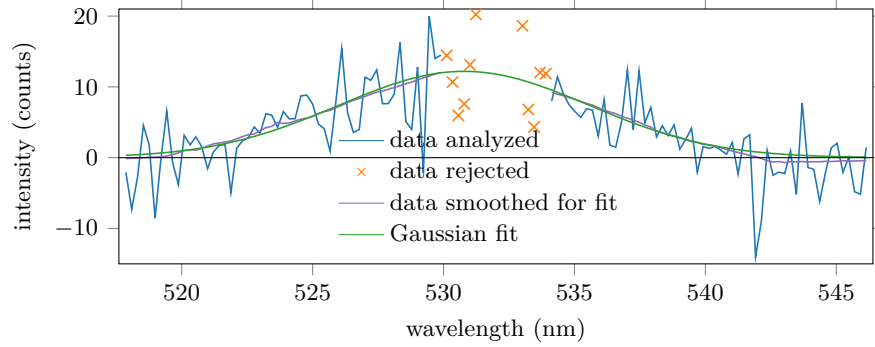


Figure 5: Thomson spectrum example obtained along the azimuthal direction with the ISCT200-GEO thruster. The corresponding electron density and temperature are  $((2.6 \pm 0.2) \times 10^{16} \text{ m}^{-3})$  and  $(20 \pm 2) \text{ eV}$  respectively. Discharge parameters are a xenon flow rate of  $1.6 \text{ mgs}^{-1}$ , discharge voltage of 250 V and a discharge current of 1.13 A. This spectrum is obtained for an axial distance from the exit plane of 4 mm and peak magnetic field of 25 mT at the exit plane.

The spectra examples provided in Fig. 14 shows cases obtained for lower electron temperatures but with wings at large spectral shifts. For these spectra the 600 lines  $\text{mm}^{-1}$  grating was used for two acquisitions, the first one centered at 532 nm) and the second one shifted of 10 nm from the laser wavelength, in the direction of the wing. The less-dispersive 2400 lines  $\text{mm}^{-1}$  grating was also used to better resolve the scattering signal from cold electron population. The procedure previously described was applied to the concatenation of these three parts of the Thomson spectrum. To compensate for the variation of the  $c_1$  coefficient between the two gratings, the data obtained with the 2400 lines  $\text{mm}^{-1}$  grating were multiplied by a normalization coefficient obtained from the Raman calibration procedure with both gratings.

#### 4. Data analysis for EEDF estimation

For the estimation of the EEDF, the spread in electron energies is estimated from the shift from the incident wavelength ( $\lambda_i$ ) using the relation

$$E = \frac{m_e c^2}{2} \left( \frac{\lambda - \lambda_i}{2\lambda_i \sin(\theta/2)} \right) \quad (3)$$

Under the hypothesis of an isotropic behavior of electron, the non-normalized EEDF can be obtained from the scattering spectrum derivative with the following expression

$$f_E(E) \propto -\text{sgn}(\lambda - \lambda_0) \frac{dI_T}{d\lambda} \quad (4)$$

With  $\text{sgn}$  the sign function giving  $-1$  for negative values of  $\lambda - \lambda_0$  and 1 for positives values.  $\lambda_0$  corresponds to the wavelength associated to the center of the Gaussian distribution fitted to the Thomson spectrum. Using  $\lambda_0$  rather  $\lambda_i$  help to respect the isotropism hypothesis even with a simple drift velocity. Finally,  $dI_T/d\lambda$  is the derivative of the signal measured from Thomson scattering with respect to the wavelength.

In practice, the derivative of the Thomson spectrum is calculated with a Savitzky-Golay filter applied to the data interpolated by the values from the Gaussian fit inside the rejection interval. The normalized EEDF ( $f_E(E)$ ) is usually obtained from the division of the distribution obtained from Eq. (4) by its integral over the energy range probed. This energy range is directly related to the spectral dynamic on the CDD with the chosen detection branch configuration. This procedure is valid only if the density of electron with energies outside the interval probed is either negligible or can be interpolated (in case of a theoretical distribution).

### III. Results and discussion

#### A. Preliminary remarks

To determine whether the electron properties are isotropic, measurements along both the radial and azimuthal directions were made by switching between the two scattering configurations presented in Section 2. In the subsequent plots, values of electron properties obtained along the azimuthal direction are plotted with blue triangles and radial observations plotted with yellow circles. While the observation of non-isotropic electron temperature or drift velocity has a physical significance, this is not the case for electron density, which is expected to be the same in both directions. Differences in the electron density measured at the azimuthal and radial positions may be due to (i) azimuthal plasma non-uniformity (possibly influenced by the cathode position or spatial inhomogeneities of the magnetic field), or (ii) slight displacement (below 0.3 mm) of the measurement position as the thruster is translated laterally to switch between the two scattering configurations.

Typically, axial exploration of electron properties was performed within the axial range 2–40 mm in the azimuthal direction and 3–40 mm in the radial direction with respect to the exit plane. The closest approach to the exit plane for both directions is that for which stray light reflections can be sufficiently attenuated for the Thomson signal to be unobscured. The difference in the closest approach for the two directions is due to the different levels of light reflected off the central pole which enter the detection branch. While with the radial scattering configuration the inner pole behind the observation volume is directly illuminated, it is not the case with the azimuthal scattering configuration. The furthest axial distance is that for which the plasma density remains sufficient for a signal to be detected. As shown with the Thomson spectrum example in Fig. 5, a Gaussian curve can be fitted to the data with confidence despite the low electron density.

#### B. Magnetic field configuration

The difference in electron properties between the standard and magnetically-shielded configurations was investigated with a fixed discharge voltage of 250 V and discharge current of 1.14 A, it leads to a discharge power of 285 W. For the ISCT200-GEO thruster, the  $B_{low}$  configuration (with the magnetic field directed towards the outer pole) were used. The discharge voltage and current fixed are achieved with a xenon flow rate of  $1.18 \text{ mg s}^{-1}$ . For the shielded ISCT200-MS operated at the same magnetic field intensity ( but directed towards the inner pole), a xenon flow rate of  $1.05 \text{ mg s}^{-1}$ ) was necessary to achieve the discharge conditions chosen.

The comparisons between the two architectures are shown in Fig. 6. As seen in the first row of Fig. 6, higher electron densities are reached with the ISCT200-MS, up to  $4 \times 10^{16} \text{ m}^{-3}$ . This difference with the ISCT200-GEO, operated at the same discharge conditions, can be explained by the downstream shift of the ionization and acceleration position<sup>27</sup> with the shielded configuration.

Electron temperature is plotted on the second row of Fig. 6. Much higher electron temperatures are found with the ISCT200-MS Hall thruster, reaching as high as 75 eV. Recent simulations also reported much higher electron temperatures with a magnetically-shielded thruster than with a standard magnetic configuration, a feature associated with a downstream shift of the axial profile.<sup>34</sup> Nevertheless, absolute values of electron temperature from Ref. 34 are lower: only 30 eV is reached with the standard configuration, while and 53 eV is attained with the MS configuration. The difference between the electron temperatures from simulations and experiments under similar conditions is yet to be understood, but it is possible that the contribution of plasma instabilities - not captured in the simulations - may contribute to electron heating to some degree.

Drift velocities for the two architectures are presented in the third row of Fig. 6. With the magnetic shielding configuration, for the scattering configuration associated with azimuthal investigation, the spectral shift of the Thomson spectra at positions near the exit plane is much more significant than for the standard architecture.

For previous measurements on a planar magnetron,<sup>24</sup> we reported sensitivity for electron drift velocity estimation as low as the velocity corresponding to the Doppler shift associated to a spectral width of one pixel (at the corresponding wavelength). This sensitivity would correspond to approximately  $100 \text{ km s}^{-1}$  with the  $600 \text{ lines mm}^{-1}$  grating and the 8-pixel wavelength binning used for this paper. Nevertheless, the Thomson scattering signal obtained from the Hall thruster plasma is more challenging to analyze because of the lower signal-to-noise ratio and distortion of the Thomson spectrum by plasma emission lines. For this reason, electron drift velocities below  $500 \text{ km s}^{-1}$  obtained in this campaign were not considered for data

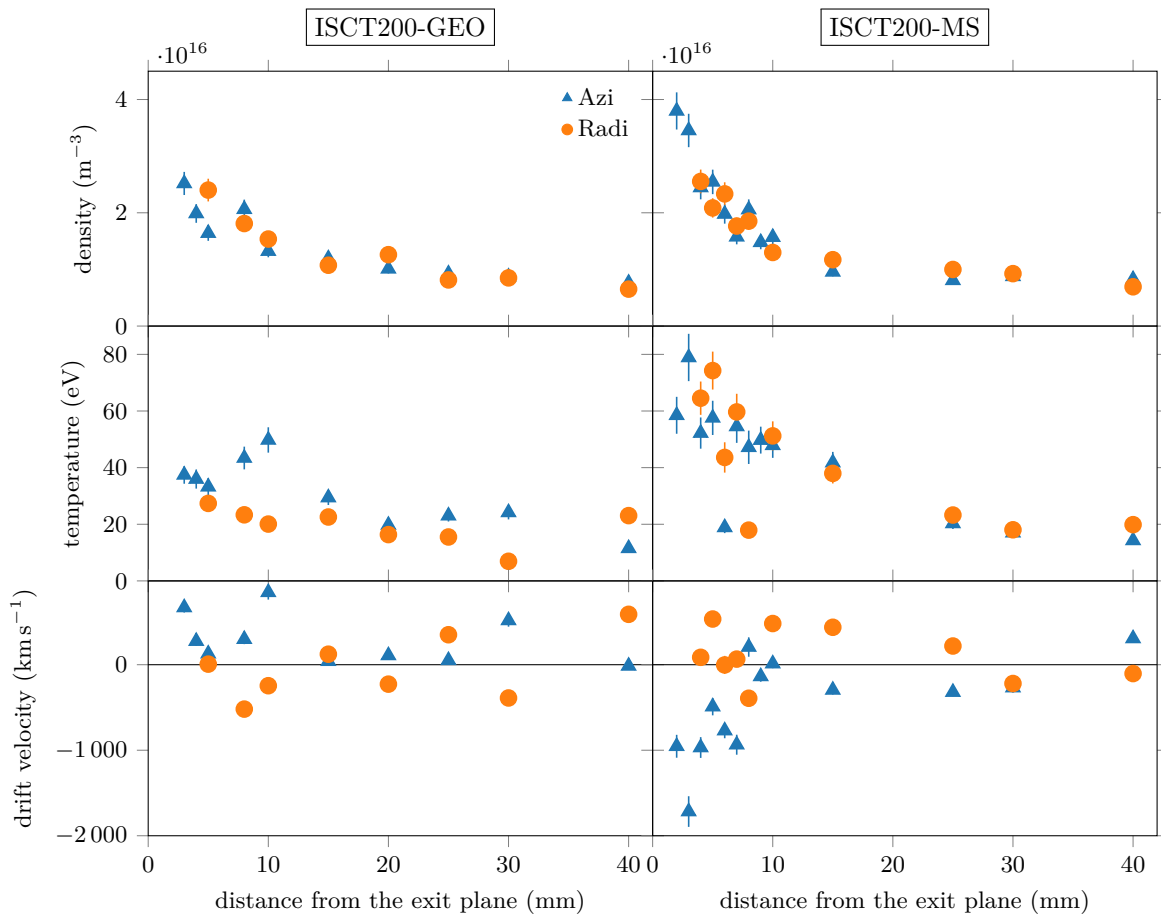


Figure 6: Comparison of electron density, temperature and and drift velocity along both azimuthal and radial directions. The discharge conditions are fixed to at 250 V and 1.14 A both magnetic field configurations: standard ISCT200-GEO (left column) and unshielded ISCT200-MS (right column)

discussions. This lower limit corresponds to the drift velocity associated with the Doppler broadening of the FWHM of the instrument profile obtained with identical acquisition parameters. Considering this limit, only the drift velocity along the azimuthal direction obtained with the ISCT200-MS and few values obtained with the ISCT200-GEO can be interpreted.

The electron drift velocity direction and magnitude along the azimuthal direction is expected to be easier to predict because the  $\vec{E} \times \vec{B}$  drift should be one of the dominant contributions in the acceleration region. Given the magnetic and electric field orientations in the acceleration region, the azimuthal drift velocity of electrons is expected to be anti-clockwise with the ISCT200-GEO (facing the ion beam) and clockwise for the ISCT200-MS. Along the radial direction, it is more difficult to predict the drift velocity trend as other contributions, such as curvature and gradient drift, may be on a similar order. With the ISCT200-GEO the electron drift velocity along the azimuthal direction is systematically positive with only a few values above the threshold of  $500 \text{ km s}^{-1}$ . As expected, these positive values correspond to electrons drifting in the clockwise direction. Along the radial direction, the drift velocity near the exit plane is weaker and oscillates around zero.

With the ISCT200-MS the azimuthal drift velocity is significantly negative close to the thruster exit plane. These negative values are due to the reversed magnetic field direction and are consistent with a clockwise  $\vec{E} \times \vec{B}$  drift. Such significant values of electron drift velocity are observable only with the ISCT200-MS because the acceleration region, where the electric field is strong, is shifted downstream, rendering it accessible to the ITS probing beam. As with the standard configuration, electron drift velocities in the radial direction are comparatively low.

### C. Discussion on the high electron temperatures observed

The results from these experiments show electron temperatures reaching easily 60 eV for certain conditions, a result which does not match any typical probe measurements on large and small thrusters, where authors have previously measured temperatures in the range of few tens of eV in the near-field region, for example in Refs. 11, 14 and in Ref. 35, where for a similar discharge voltage in a larger thruster, the electron temperature is only 30 eV in the acceleration region.

We first consider examples of temperatures in the 60 eV range, using spectra obtained on the ISCT200-MS 2 mm from the exit plane with two magnetic field directions. The same discharge condition as Section B were used for the case with the magnetic field directed towards the inner pole (first row in Fig. 7). For the case with the magnetic field directed towards the outer pole (second row in Fig. 7), the xenon flow was adjusted to  $1.2 \text{ mg s}^{-1}$  to reach the same discharge current and voltage. The corresponding electron properties, deduced from Gaussian fits to these spectra, are shown in the legend of Fig. 7.

The following observations may be made:

- (i) The presence of a strong electron drift shifts the center of the spectrum away from the laser frequency, and a switch in the magnetic field direction (from directed outwards to inwards) also switches the direction of this shift. This is visible in Fig. 7.
- (ii) In addition to the spectral shift, the spectra are asymmetric. A long tail is visible along the spectral direction associated with the electron drift velocity, while the opposite side of the spectrum shows a fast decrease of signal intensity. This suggests that the electrons are not in thermal equilibrium. While a Gaussian fit may not be strictly relevant, it can still reasonably fit one side of the spectrum, and the electron temperature is estimated from such a fit. The spectra shown, though much noisier than the example provided in Fig. 5, are still sufficiently well-resolved to show their wide spectral range.
- (iii) Lastly, we consider challenges associated with the analysis of these spectra. The high-electron temperature, low-electron density regime of the cases shown results in low-amplitude, broad Thomson spectra. These spectral features, combined with the presence of several residual emission lines, contribute to the noisiness of the data. In spite of this, the large spectral width of the cases shown is unambiguous.

What contributes to this relatively large width? We may speculate that this observation is due to oscillatory discharge behavior, averaged out during the 10-minute acquisition time for each spectrum. Although we have sought to limit these investigations to regimes in which the discharge current standard deviation is low, this does not rule out the possible influence of high-frequency plasma instabilities<sup>36</sup> which may generate electric field fluctuations. The accelerating potential is not truly stationary. This may create oscillations in the bulk distribution which, when averaged, would appear as unusually broad spectra, leading to an higher electron temperatures estimated than would be expected from the average applied potential. To avoid this,

it would be necessary to obtain a highly time-resolved measurement (ideally, a single shot measurement with shorter laser pulse duration), at present beyond reach for these low plasma densities. In addition to this effect, high-frequency instabilities have been demonstrated to contribute to true electron heating in thrusters. This dynamic heating is discussed in a number of works, including in Ref. 37, where electron temperatures reaching the 100 eV range have been mentioned. It is worth noting that these simulations do not fully account for the energy dissipation mechanisms for electrons. Nevertheless, a full understanding of the contribution of plasma oscillations to the experimentally-measured spectral widths may be achievable through numerical modeling, to be examined in future work.

Further insights into electron behavior at high temperature may be obtained from the calculation of the electron velocity distribution function from the Thomson spectrum profile.<sup>38</sup> This calculation requires a higher signal-to-noise ratio, as discussed in Ref. 23, this condition is obtained only with discharge leading to much colder electrons (see Section 2).

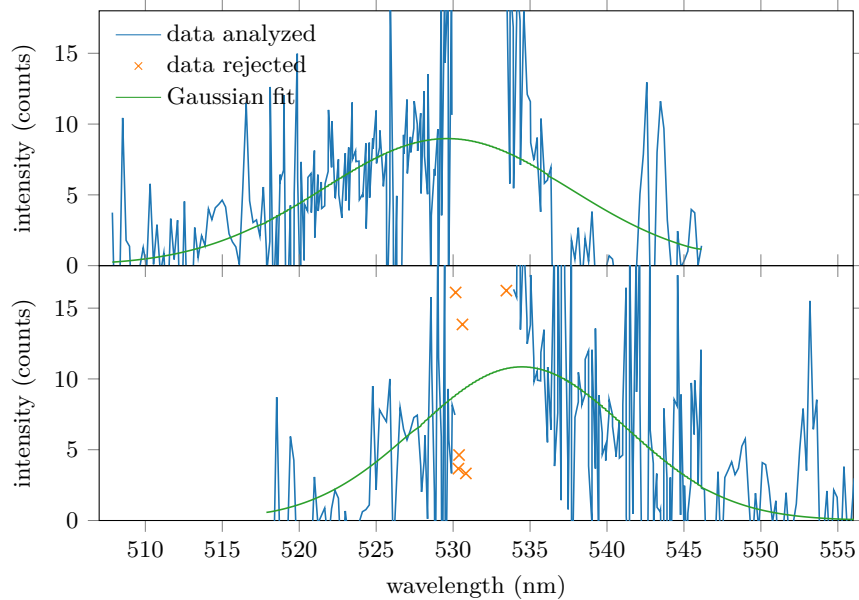


Figure 7: Thomson spectra obtained along the azimuthal direction 2 mm from the exit plane of the ISCT200-MS thruster, for 250 V discharge voltage and 1.14 A discharge current. Top: magnetic field directed towards the inner magnetic pole;  $n_e=(3.5 \pm 0.2) \times 10^{16} \text{ m}^{-3}$ ,  $T_e=(58 \pm 7) \text{ eV}$  and  $v_{e,drift}=(-950 \pm 130) \text{ km s}^{-1}$ . Bottom: magnetic field directed towards the outer magnetic pole;  $n_e=(3.8 \pm 0.3) \times 10^{16} \text{ m}^{-3}$ ,  $T_e=(41 \pm 4) \text{ eV}$  and  $v_{e,drift}=(1000 \pm 100) \text{ km s}^{-1}$ .

#### D. Influence of the discharge voltage

Lastly, a study of the influence of the discharge voltage on the electron properties was performed, at a fixed position 2 mm from the exit plane. Observations were made along the azimuthal direction. The discharge voltage was varied from 112 V to 300 V at constant discharge power of 300 W, with an adjustment of the xenon mass flow rate from  $2.3 \text{ mg s}^{-1}$  to  $0.9 \text{ mg s}^{-1}$ . The investigations were performed on the ISCT200-MS with the magnetic field directed toward the external pole. At the axial position probed, electron drift velocity is expected to be dominated by the  $\vec{E} \times \vec{B}$  contribution, giving an anti-clockwise rotation of electrons (i.e., the estimation of a positive electron drift velocity).

As seen in Fig. 8, the electron density is significantly lower at higher discharge voltages. This trend might be expected from the decrease in xenon mass flow rate imposed in order to maintain the discharge power at 300 W when the voltage is increased.

Provided most of the voltage drop has occurred at the position probed, the ion velocity  $v_i$  can be expressed as  $\approx \sqrt{qU_d/m_i}$ , where  $U_d$  is the discharge voltage and  $q$  is the charge state of the ion (we will consider only singly charge ions with  $q = e$ ). This velocity is linked to the ion density through the expression of the xenon mass flow rate. At a given position and under the quasi-neutrality hypothesis, the electron density can be

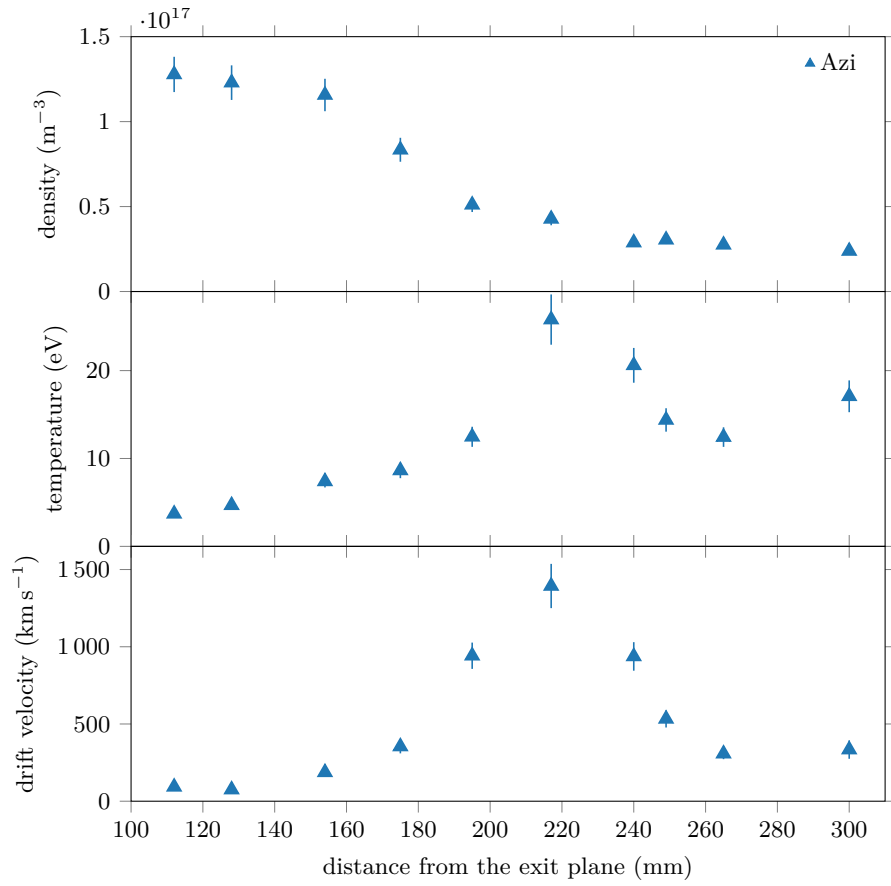


Figure 8: Electron density, temperature and drift velocity along the azimuthal direction 2 mm from the exit plane for the ISCT200-MS thruster. Various discharge voltages were investigated at a fixed power of 300 W.

estimated from this ion velocity through the formula

$$n_e = \frac{\eta_{prop} \dot{m}_n}{m_i A v_i} \quad (5)$$

where  $\dot{m}_n$  is the mass flow rate of xenon atoms through a given section  $A$ .  $\eta_{prop}$  is the propellant utilization efficiency.  $m_i$  and  $v_i$  correspond to, respectively, the mass xenon ions and their velocity along the axial direction.

From the injection of the ion velocity expression in Eq. (5), and under the hypothesis of a constant ionization efficiency and divergence angle, the coefficient  $n_e \sqrt{U_d}$  is expected to be proportional to the xenon mass flow rate  $\dot{m}_n$ . For constant discharge power (i.e., for a fixed value of the product  $\dot{m}_n U_d$  as  $I_d \propto \dot{m}_n$ ),  $n_e U_d^{3/2}$  should be a constant ( $c$ ). In practice, we observed that the value of  $c$  is slightly lower at 300 V than at 112 V; this is likely due to a slight downstream axial shift in the accelerating electric field profile, or potentially, an increase in the propellant efficiency<sup>39</sup> as the voltage is increased.

The relatively large electron densities obtained with the ISCT200-MS at low discharge voltages facilitate the analysis of the Thomson signal. Near the exit plane, quantitative deviations from the typical Gaussian form of the Thomson spectra were also observed at low voltages, these deviations are discussed in Section E from an axial exploration at a low discharge voltage.

The variation in electron temperature shown in Fig. 8 is non-monotonic. At low discharge voltage, electron temperature first rises linearly from 8 eV to 13 eV before a fast increase to 25 eV at 217 V, followed by a slow decrease to around 15 eV at higher voltages.

Previous studies<sup>40</sup> using probes investigated the influence of channel width and discharge voltage on the maximum electron temperature. It was reported that regardless of the channel width, a linear increase of the maximum electron temperature was observed at low discharge voltages, with saturation in temperature observed around 60 eV at large discharge voltages.

The trend of the electron temperature can best be interpreted by considering the effect of varying voltage on the position of the peak electric field. There appears to be a tendency for the electric field get broader and shift further outwards as the discharge voltage decreases.<sup>7,41</sup> If the electron temperature is correlated (as it is expected<sup>34</sup>) with drift velocity, then the peak in the temperature at 217 V is apparent because for this voltage, the peak electric field position coincides with the observation volume position 2 mm from the exit plane. The subsequent decrease in the electron temperature at higher voltages would merely be due to the peak electric field moving upstream of the observation volume position.

At a position 2 mm from the exit plane, the electron drift velocity is dominated by the  $\vec{E} \times \vec{B}$  contribution, and thus the electric field is proportional to the azimuthal drift velocity. This accounts for why the trend in electron drift velocity shown in Fig. 8 is similar to that of the electron temperature, which, as we have discussed, depends on the electric field. As with the electron temperature, the drift velocity profile is a reflection of the progressive axial shift of the peak electric field into, and then out of, the fixed observation volume.

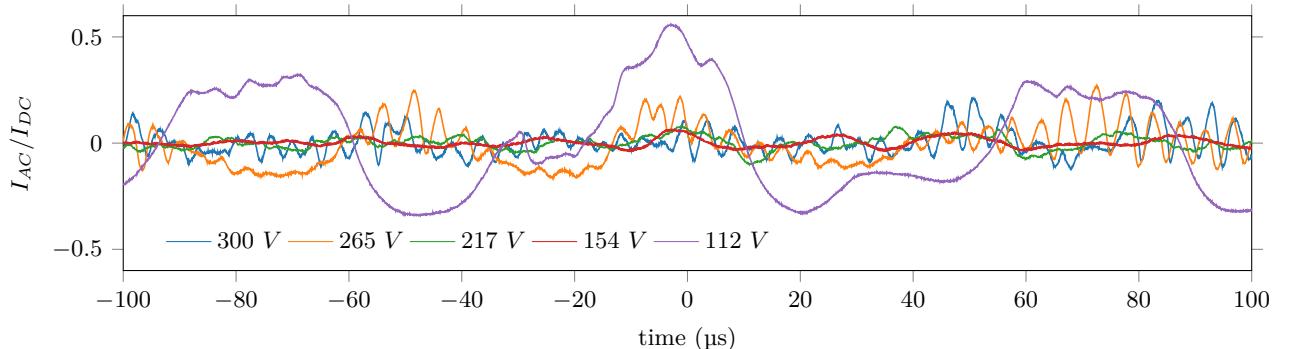


Figure 9: AC component of the discharge current for different discharge voltages for the ISCT200-MS thruster. The DC component of the current is 1.14 A.

The temporal profiles and power density spectra of the discharge current for several discharge voltages are shown in Fig. 9 and Fig. 10. The discharge current main oscillations are in the  $2 \times 10^5$  Hz range at

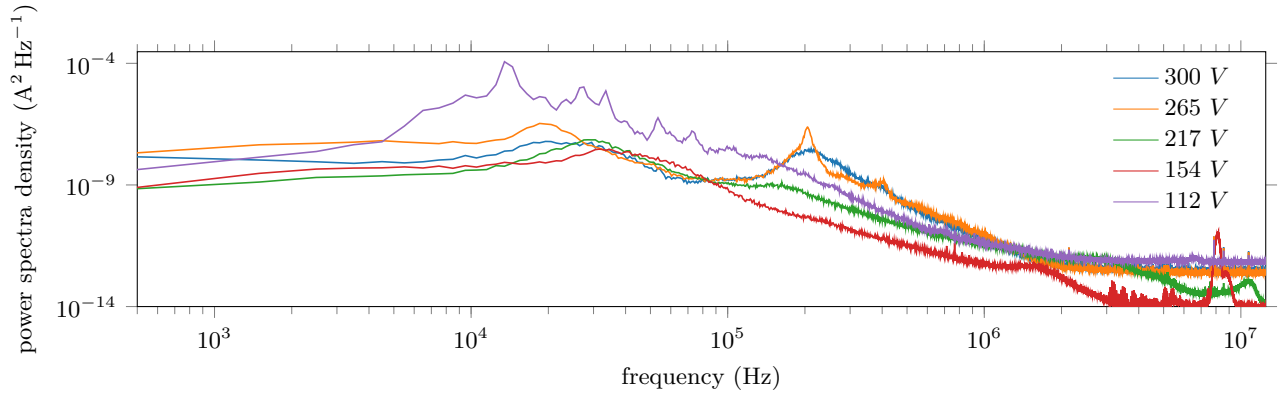


Figure 10: Power density spectra of the discharge current for different discharge voltages for the ISCT200-MS thruster, for the same conditions as Fig. 9.

higher discharge voltage and may be consistent with transit time oscillations. At lower discharge voltages, oscillations in the discharge current are more concentrated in the  $4 \times 10^4$  Hz (breathing mode) range. At the lowest discharge voltage of 112 V, current oscillations are significant with a peak-to-peak amplitude as large as the mean current, with rotating spokes expected to appear.<sup>42,43</sup> With this discharge mode, the power spectra of the oscillations cover a broadband in the  $10^4$  Hz range, but with well-defined oscillations, synchronization of the Thomson signal acquisition with different points in the discharge current period appears achievable, it would give access to time-resolved measurements of the electron properties.

At intermediate discharge voltage, near 217 V, there is a minimum in the power density integrated over the entire frequency range, yet the measured electron temperature is maximum for this voltage. As discussed previously, it is not yet possible to rule out the contributions of high-frequency instabilities (not visible in the discharge current measurement) to the apparent high electron temperatures.

Overall, modifications of the discharge conditions when the discharge voltage is varied will change both electron properties and contribute to the electric field axial shift phenomenon discussed previously.

### E. Explorations at low discharge voltage

For a better characterization of the electron properties at a low discharge voltage, an axial exploration was realized. In this section, we focus on the plasma of an ISCT200-MS with the  $B_{low}$  configuration and the magnetic field lines directed towards the inner pole of the thruster. The discharge voltage was fixed at 150 V, the lower thermal load on the thruster at low discharge voltages enable operation of the thruster at higher power than at high voltage. That is why we operated with a discharge current up to 2.17 A, it corresponds to a discharge power of 325 W. These discharge conditions were obtained with a xenon flow rate of  $2.1 \text{ mg s}^{-1}$ .

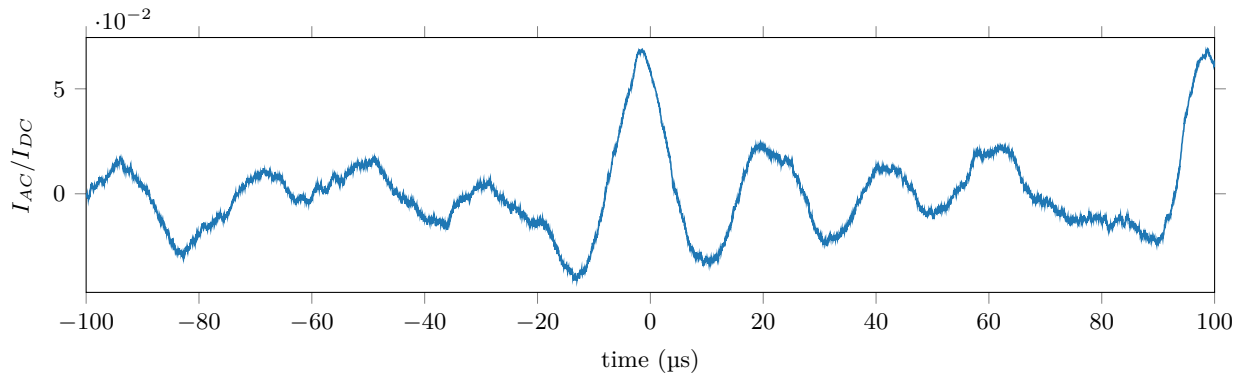


Figure 11: AC component of the discharge current for the ISCT200-MS operating under a voltage of 150 V and a xenon flow rate of  $2.1 \text{ mg s}^{-1}$ . The DC component of the current is 2.17 A.

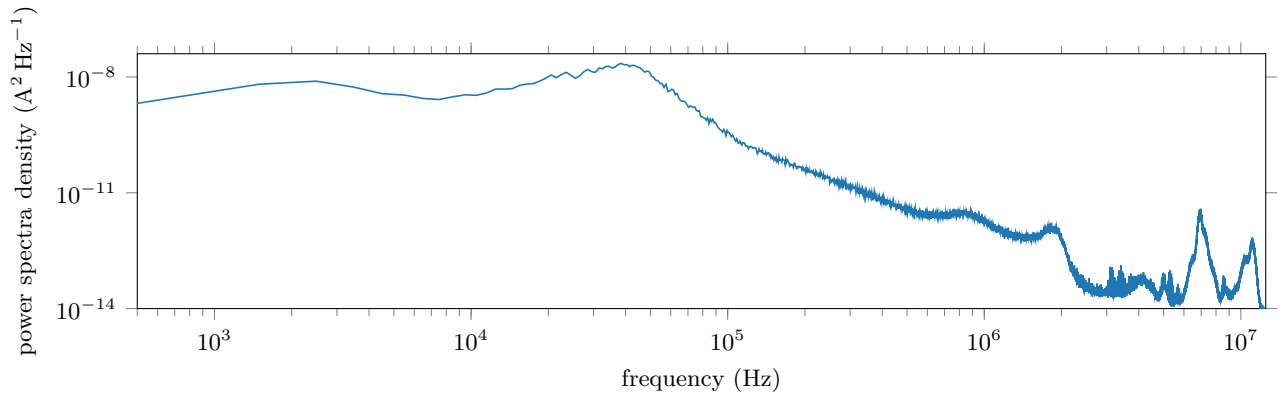


Figure 12: Power density spectra of the discharge current whose temporal trace is shown in Fig. 11.

As shown in Fig. 11 and Fig. 12 the temporal behavior of the discharge current with the discharge conditions chosen is very close to the one observed during the discharge voltage exploration at 157 V (see Fig. 9 and Fig. 10). Despite a 14 % increase in discharge power, the same broad peak around  $5 \times 10^4$  Hz and sharp peak at frequencies just below  $10^7$  Hz are observed with both discharge conditions.

### 1. Axial exploration

The results from the axial exploration in the middle of the ISCT200-MS channel are presented in Fig. 13. The profile was realized for distances from the exit plane ranging from 2 mm to 20 mm for the scattering configuration associated with azimuthal investigations and from 4 mm to 20 mm with the scattering configuration associated with radial investigations.

The axial profile of electron density obtained with the ISCT200-MS at 150 V (first row of Fig. 13) is much higher than the one obtained at 250 V (second column, first row of Fig. 6). This can be explained by the higher mass flow rate of xenon injected and to the less efficient acceleration of ions, these contributions add up and lead to higher density. A comparison with the density obtained from the discharge voltage exploration at 157 V (at 2 mm from the exit plane) shows that the electron density were higher during the axial profile exploration ( $1.6 \times 10^{17} \text{ m}^{-3}$  at 150 V versus  $1.2 \times 10^{17} \text{ m}^{-3}$  at 157 V). This higher density can be explained by the 14 % increase in discharge power used during the axial exploration. The steep increase close from the exit plane suggests that we may have probed the end of the ionization region and the beginning of the acceleration region.

For the electron temperature, for the first time, we observed a clear increase in the temperature with increasing distances from the exit plane of the thruster. The temperature increases almost linearly from 1.5 mm to 3 mm where it reaches a plateau below 40 eV and then decreases progressively from 6 mm to 20 mm from the exit plane. This increase of electron temperature suggests that we probed electron feeling the increasingly high electric field of the acceleration region.

Inside the region with a linear increase of electron temperature, we measured along the azimuthal direction, Thomson spectra with strongly non-Gaussian shapes. For these spectra, with an example shown in the first row Fig. 14 for a distance of 2 mm from the exit plane, the reliability of a Gaussian fit could be criticized. That is why we used an alternative method, based on the analysis of the Thomson spectrum distribution, for an estimation of the electron temperature and drift velocity. To the data analyzed, interpolated by the Gaussian fit values inside the rejection interval, we applied a Savitzky-Golay filter to smooth the Thomson distribution and obtain an analytic function. From this distribution, we were able to estimate the mean ( $\lambda_{0,d}$ ) and standard deviation ( $\Delta\lambda_d$ ) of the distribution and calculate the associated electron temperature and drift velocity with Eq. (2). The values obtained from this method are shown with square markers in Fig. 13.

The electron temperature obtained from the analysis of the Thomson spectrum distribution is usually much higher. For example, at 2 mm from the exit plane, the Gaussian fit method gives 7.8 eV while the distribution method gives 27 eV. This large difference comes from the wings at large wavelength shifts that are not taken into consideration with the shape of the Gaussian fit. This Thomson spectrum distribution does

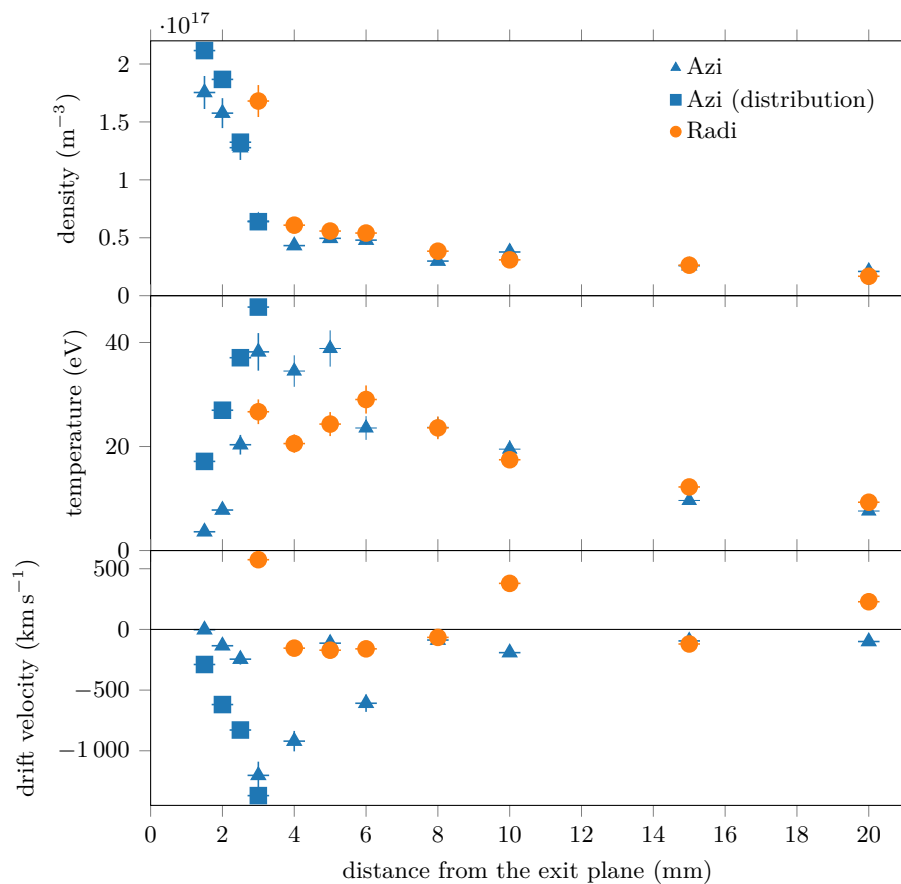


Figure 13: Electron temperature, density and drift velocity obtained from an axial exploration inside the plasma of an ISCT200-MS operating at 150 V and 2.17 A with a xenon flow rate of  $2.1 \text{ mg s}^{-1}$ . The “Azi” and “Radi” values are obtained from the parameters of the Gaussian fit applied to the spectrum acquired with the azimuthal and radial scattering configuration respectively. The “Azi (distribution)” values are obtained from an analysis of the Thomson spectrum distribution.

not correspond to any canonical shapes and highlights the fact that electrons are out of thermal equilibrium at these positions.

The electron drift velocities obtained at 150 V are lower than the one obtained with a discharge voltage of 250 V. Still, if we consider that the drift comes mainly from the  $\vec{E} \times \vec{B}$  contribution, the decrease is less significant than expected if only a cross-multiplication were applied. The linear increase of the drift velocity up to  $-1200 \text{ km s}^{-1}$  can be explained by the fact that we were probing a broader acceleration region, more shifted downstream in comparison to the case at 250 V. This was already observed from LIF measurements in Hall thrusters discharges operated at various voltages.<sup>7,41</sup> Similarly to the temperature, the electron drift velocity estimated from the mean of the spectrum distribution is much higher than the value estimated from the Gaussian fit. The tails on the spectrum, associated with highly energetic electrons, is again at the origin of this disparity.

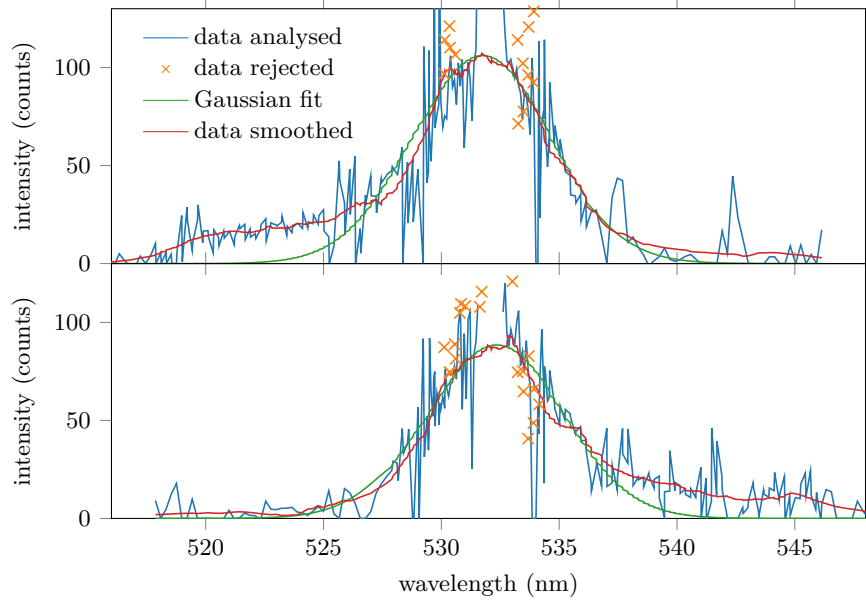


Figure 14: Thomson spectra obtained along the azimuthal direction 2 mm from the exit plane of the ISCT200-MS, for a discharge voltage of 150 V and a discharge current of 2.17 A. Top: magnetic field lines directed towards the inner pole (i.e., the same condition as for Fig. 13); the Gaussian fit gives  $n_e = (1.6 \pm 0.1) \times 10^{17} \text{ m}^{-3}$ ,  $T_e = (7.9 \pm 0.7) \text{ eV}$  and  $v_{e,drift} = (130 \pm 20) \text{ km s}^{-1}$ . Bottom: magnetic field directed towards the outer magnetic pole (the xenon mass flow rate were adjust to  $2.15 \text{ mg s}^{-1}$  to keep the discharge current at the nominal value); The Gaussian fit gives  $n_e = (1.3 \pm 0.1) \text{ m}^{-3}$ ,  $T_e = (7.4 \pm 0.7) \text{ eV}$  and  $v_{e,drift} = (110 \pm 20) \text{ km s}^{-1}$ .

## 2. Electron Energy Distribution Function derivation

As previously mentioned, the use of a magnetically shielded thruster at low discharge voltage allows respectively a downstream shift of the acceleration regime and an increase of the electron density (i.e., an increased signal from Thomson scattering and the ability to probe the acceleration region). These experimental conditions are well-inclined towards the observation of a clear deviation of the Thomson spectrum from a Gaussian distribution. Such distortions do not come from imperfect subtraction of the plasma emission records. As shown in Fig. 14, at similar discharge condition, but with a reversed magnetic field, the spectral side associated with the non-Gaussian tail reverse. This observation shows that this distortion has a physical meaning which is linked to the direction of the  $\vec{E} \times \vec{B}$  drift.

Because the shape of the Thomson spectrum does not follow any canonical distribution (fully defined with the temperature and drift velocity), it becomes less relevant to try to fit it with a given function. Instead, it is more pertinent to estimate the EEDF associated with this spectrum shape. From the method presented in Section 4 the EEDF associated to the spectra of Fig. 14 were calculated and are shown in Fig. 15. With a green line is shown the EEDF obtained from the Gaussian function used for the fitting (i.e., under the hypothesis of thermal equilibrium). This analytic function was normed so that its integral gives one. The

red line represents the experimental EEDF obtain from the derivative of the smoothed Thomson spectrum shape. To ease the comparison, this function was multiplied by a coefficient so that both the red and green lines have the same maximal value.

For both directions of the magnetic field, the experimental EEDF obtained exhibit a shape not symmetric relative to the vertical line at 0 eV.

Along the direction associated with the  $\vec{E} \times \vec{B}$  drift, dips inside the low energy part make the density for some energy range lower than in the case of thermal equilibrium. On the contrary, for the high energy part, a hump around 40 eV makes the density higher than the case at thermal equilibrium for both magnetic field directions. The other humps visible around 80 eV may have a physical meaning, however, the decreased signal to noise ratio associated to these spectral shifts (at the end of the tail at 13 nm from the laser wavelength) would make its interpretation less trustworthy.

Along the opposite direction, for both magnetic field directions, the distributions follow the shape expected when electrons at thermal equilibrium are considered.

In Ref. 14, investigations on the ISCT200-GEO at 200 V, with Langmuir probes installed on a fast-moving translation stage, were also used to estimate the electron energy distribution. Despite the different discharge conditions, they also observed multiple humps in the distribution with one at 40 eV. This hump they observed at 40 eV, for a distance of  $-0.9$  mm from the exit plane, were explained by electrons that would be produced inside the thruster channel and subsequently accelerated by the electric field of the acceleration region (positioned inside the channel for the ISCT200-GEO). With our ITS diagnostic, we needed investigation on the ISCT200-MS, with the acceleration region outside the exit plane, to be able to probe the corresponding EEDF. As with Langmuir probe measurement, we observed multiple humps in the distribution with also a hump at 40 eV for both magnetic field direction. These multiple humps in the energy distribution of electron seem to be characteristic of the acceleration region, independently of the thruster design and discharge voltage. However, the number and exact position of the humps seems difficult to predict. As shown in Fig. 15, with the discharge conditions unchanged, even a simple reverse of the magnetic field direction can affect the position of some humps.

As a reminder, the procedure used for estimation of the EEDF were made under the hypothesis of electrons with isotropic behavior. The large drift velocity observed and the absence of symmetry inside the EEDF derived shows that this hypothesis may not be respected any more. Still the distribution associated to displacement in the “negative direction” (i.e., negative spectral shift) and “positive direction” (i.e., positive spectral shift) are shown. Indeed, it remains an efficient way to sense the anisotropic behavior of electrons. It is a unique feature of ITS diagnostic, it not possible with other diagnostic such as Langmuir probes. Only the estimation of the one-dimensional electron velocity distribution function (1D-EVDF) needs a less restrictive hypothesis based on the independence of the electron behavior along the probed direction from the other orthogonal directions. Under this hypothesis the 1D-EVDF is directly proportional to the Thomson spectrum distribution, however, such a distribution is less general and not commonly used by the community.

## IV. Conclusion

In this paper, implementations of the recently-developed Thomson scattering diagnostic known as THETIS to Hall thruster investigations were presented. These studies focused on the determination of electron properties in two architectures of a 200 W thruster: a standard configuration and unshielded configuration. Electron properties - temperature, density, and drift velocity - were systematically measured along both the azimuthal and radial directions.

Investigations of electron properties on the standard Hall thruster revealed axial profiles of electron densities in the  $10^{16} \text{ m}^{-3}$  range and temperatures around 25 eV. Electron properties measured on the magnetically-shielded equivalent thruster confirmed (i) the axial shift of the plasma in comparison to the standard architecture, seen in higher densities downstream of the exit plane, and (ii) large and significant non-isotropic electron drift velocities, up to  $1800 \text{ km s}^{-1}$  near the thruster exit plane. Reversal of the magnetic field was found to produce a reversal of the dominant  $\vec{E} \times \vec{B}$  drift component at the exit plane. Discharge voltage explorations performed at a fixed axial position and discharge power revealed electron properties consistent with a shift in the electric field profile with voltage. With the shielded configuration, the high plasma density obtained at low discharge voltage allowed the estimation of the EEDF inside the acceleration region. These distribution functions exhibit strongly no symmetric behaviors with well-identified populations of electrons at various energies.

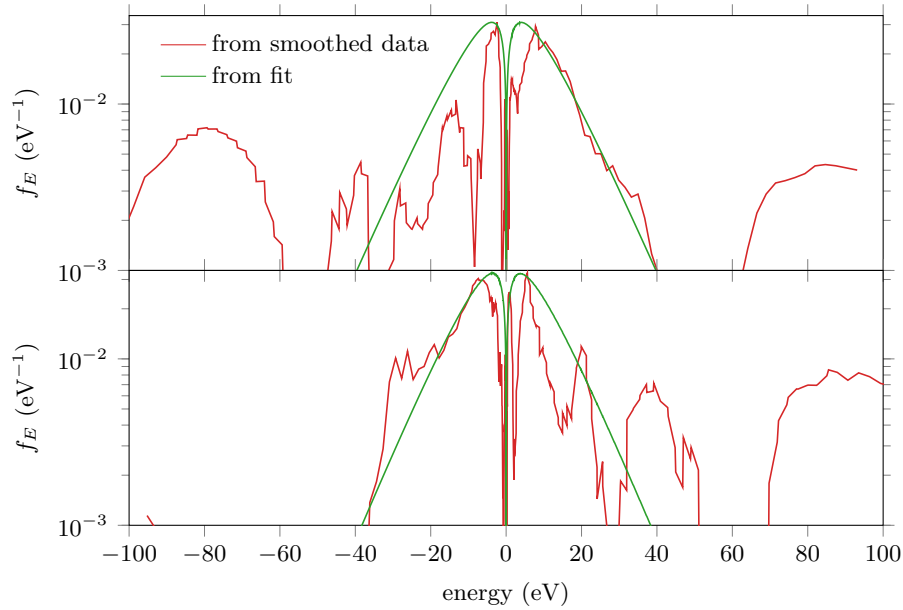


Figure 15: Estimated EEDF obtain from the Thomson spectra presented in Fig. 14. The green lines correspond to the spectrum obtain from the theoretical Gaussian fit. The red lines are the EEDF obtained from the derivative of the smoothed shape of the Thomson spectra. Top: magnetic field lines directed towards the inner pole. Bottom: magnetic field directed towards the outer pole.

## Acknowledgments

This work was supported by the French Space Agency (CNES) under the grant R & T R-S18/PF-0005-105. The authors would like to thank T. Minea, J. Fils, J. Schwindling, O. Tuske, and G. Largeau.

## References

- <sup>1</sup>Choueiri, E. Y., “A Critical History of Electric Propulsion: The First 50 Years (1906-1956),” *Journal of Propulsion and Power*, Vol. 20, No. 2, mar 2004, pp. 193–203.
- <sup>2</sup>Kim, V., Kozubsky, K., Murashko, V. M., and Semekin, A., “History of the Hall Thrusters Development in USSR,” *30th International Electric Propulsion Conference*, 2007, pp. 17–20.
- <sup>3</sup>Mazouffre, S., “Electric propulsion for satellites and spacecraft: established technologies and novel approaches,” *Plasma Sources Science and Technology*, Vol. 25, No. 3, jun 2016, pp. 033002.
- <sup>4</sup>Boeuf, J.-p., “Tutorial: Physics and modeling of Hall thrusters,” *Journal of Applied Physics*, Vol. 121, No. 1, jan 2017, pp. 011101.
- <sup>5</sup>Choueiri, E. Y., “Plasma oscillations in Hall thrusters,” *Physics of Plasmas*, Vol. 8, No. 4, 2001, pp. 1411–1426.
- <sup>6</sup>Bugrova, A., “Electron distribution function in the channel of an electron-ring plasma accelerator.pdf,” *Sov. Phys. Tech. Phys.*, Vol. 32, No. 1111, 1987.
- <sup>7</sup>Giono, G., Gudmundsson, J. T., Ivchenko, N., Mazouffre, S., Dannenmayer, K., Loubère, D., Popelier, L., Merino, M., and Olentšenko, G., “Non-Maxwellian electron energy probability functions in the plume of a SPT-100 Hall thruster,” *Plasma Sources Science and Technology*, Vol. 27, No. 1, dec 2018, pp. 015006.
- <sup>8</sup>Barral, S., Makowski, K., Peradzyński, Z., Gascon, N., and Dudeck, M., “Wall material effects in stationary plasma thrusters. II. Near-wall and in-wall conductivity,” *Physics of Plasmas*, Vol. 10, No. 10, 2003, pp. 4137–4152.
- <sup>9</sup>Sydorenko, D., Smolyakov, A., Kaganovich, I., and Raiteses, Y., “Kinetic simulation of secondary electron emission effects in Hall thrusters,” *Physics of Plasmas*, Vol. 13, No. 1, jan 2006, pp. 014501.
- <sup>10</sup>Tsikata, S., Héron, A., and Honoré, C., “Hall thruster microturbulence under conditions of modified electron wall emission,” *Physics of Plasmas*, Vol. 24, No. 5, may 2017, pp. 053519.
- <sup>11</sup>Raiteses, Y., Staack, D., Keidar, M., and Fisch, N. J., “Electron-wall interaction in Hall thrusters,” *Physics of Plasmas*, Vol. 12, No. 5, may 2005, pp. 057104.
- <sup>12</sup>Shastry, R., Gallimore, A., and Hofer, R., “Near-Wall Plasma Properties and EEDF Measurements of a 6-kW Hall Thruster,” *45th AIAA/ASME/SAE/ASEE Joint Propulsion Conference & Exhibit*, No. August, American Institute of Aeronautics and Astronautics, Reston, Virginia, aug 2009, pp. 1–15.
- <sup>13</sup>Dannenmayer, K., Kudrna, P., Tichý, M., and Mazouffre, S., “Time-resolved measurements of plasma properties using

- electrostatic probes in the cross-field discharge of a hall effect thruster,” *Contributions to Plasma Physics*, Vol. 53, No. 1, 2013, pp. 63–68.
- <sup>14</sup>Tichý, M., Pétin, A., Kudrna, P., Horký, M., and Mazouffre, S., “Electron energy distribution function in a low-power Hall thruster discharge and near-field plume,” *Physics of Plasmas*, Vol. 25, No. 6, jun 2018, pp. 061205.
- <sup>15</sup>Chiu, Y. H., Austin, B. L., Williams, S., Dressler, R. A., and Karabadzak, G. F., “Passive optical diagnostic of Xe-propelled Hall thrusters. I. Emission cross sections,” *Journal of Applied Physics*, Vol. 99, No. 11, jun 2006, pp. 113304.
- <sup>16</sup>Karabadzak, G. F., Chiu, Y. H., and Dressler, R. A., “Passive optical diagnostic of Xe propelled Hall thrusters. II. Collisional-radiative model,” *Journal of Applied Physics*, Vol. 99, No. 11, 2006.
- <sup>17</sup>Sommerville, J. and King, L., “An Optical Diagnostic for Xenon Hall Thrusters Including Metastable Contributions,” *42nd AIAA/ASME/SAE/ASEE Joint Propulsion Conference & Exhibit*, No. July, American Institute of Aeronautics and Astronautics, Reston, Virginia, jul 2006, pp. 1–9.
- <sup>18</sup>Spektor, R. and Beiting, E. J., “Non-Invasive Plasma Diagnostic Inside A Hall Thruster Discharge,” *IEPC-2007*, 2007, pp. 1–9.
- <sup>19</sup>Grimaud, L., Pétin, A., Vaudolon, J., and Mazouffre, S., “Perturbations induced by electrostatic probe in the discharge of Hall thrusters,” *Review of Scientific Instruments*, Vol. 87, No. 4, apr 2016, pp. 043506.
- <sup>20</sup>Tsikata, S., *Small-scale electron density fluctuations in the Hall thruster, investigated by collective light scattering*, Ph.D. thesis, Ecole Polytechnique, 2009.
- <sup>21</sup>Washesleski, R. L., *Laser Thomson scattering measurements of electron temperature and density in a Hall-effect plasma*, Ph.D. thesis, Michigan Technological University, 2012.
- <sup>22</sup>Washesleski, R. L., Meyer, E. J., and King, L. B., “Application of maximum likelihood methods to laser Thomson scattering measurements of low density plasmas,” *Review of Scientific Instruments*, Vol. 84, No. 10, oct 2013, pp. 105101.
- <sup>23</sup>Vincent, B., Tsikata, S., Mazouffre, S., Minea, T., and Fils, J., “A compact new incoherent Thomson scattering diagnostic for low-temperature plasma studies,” *Plasma Sources Science and Technology*, Vol. 27, No. 5, may 2018, pp. 055002.
- <sup>24</sup>Tsikata, S., Vincent, B., Minea, T., Revel, A., and Ballage, C., “Time-resolved electron properties of a HiPIMS argon discharge via incoherent Thomson scattering,” *Plasma Sources Science and Technology*, Vol. 28, No. 3, mar 2019, pp. 03LT02.
- <sup>25</sup>Lejeune, A., Dannenmayer, K., Bourgeois, G., Mazouffre, S., Guyot, M., and Denise, S., “Impact of the channel width on Hall thruster discharge properties and performances,” *IEPC-2011*, 2011, pp. 1–15.
- <sup>26</sup>Mazouffre, S., Bourgeois, G., Dannenmayer, K., and Lejeune, A., “Ionization and acceleration processes in a small, variable channel width, permanent-magnet Hall thruster,” *Journal of Physics D: Applied Physics*, Vol. 45, No. 18, may 2012, pp. 185203.
- <sup>27</sup>Grimaud, L. and Mazouffre, S., “Ion behavior in low-power magnetically shielded and unshielded Hall thrusters,” *Plasma Sources Science and Technology*, Vol. 26, No. 5, apr 2017, pp. 055020.
- <sup>28</sup>Grimaud, L. and Mazouffre, S., “Performance comparison between standard and magnetically shielded 200 W Hall thrusters with BN-SiO<sub>2</sub> and graphite channel walls,” *Vacuum*, Vol. 155, No. June, sep 2018, pp. 514–523.
- <sup>29</sup>Mikellides, I., Katz, I., Hofer, R., Goebel, D., de Grys, K., and Mathers, A., “Magnetic Shielding of the Acceleration Channel Walls in a Long-Life Hall Thruster,” *46th AIAA/ASME/SAE/ASEE Joint Propulsion Conference & Exhibit*, American Institute of Aeronautics and Astronautics, Reston, Virginia, jul 2010, pp. 1–25.
- <sup>30</sup>Conversano, R. W., Goebel, D. M., Hofer, R. R., Matlock, T. S., and Wirz, R. E., “Development and Initial Testing of a Magnetically Shielded Miniature Hall Thruster,” *IEEE Transactions on Plasma Science*, Vol. 43, No. 1, jan 2015, pp. 103–117.
- <sup>31</sup>de Grys, K., Mathers, A., Welandar, B., and Khayms, V., “Demonstration of 10,400 Hours of Operation on 4.5 kW Qualification Model Hall Thruster,” *46th AIAA/ASME/SAE/ASEE Joint Propulsion Conference and Exhibit*, No. July, American Institute of Aeronautics and Astronautics, Reston, Virginia, jul 2010.
- <sup>32</sup>Ernst, W. E., Softley, T. P., and Zare, R. N., “Stark-effect studies in xenon autoionizing Rydberg states using a tunable extreme-ultraviolet laser source,” *Physical Review A*, Vol. 37, No. 11, jun 1988, pp. 4172–4183.
- <sup>33</sup>Jiang, T., Bowden, M. D., Wagenaars, E., Stoffels, E., and Kroesen, G. M., “Diagnostics of electric fields in plasma using Stark spectroscopy of krypton and xenon atoms,” *New Journal of Physics*, Vol. 8, 2006.
- <sup>34</sup>Garrigues, L., Santhosh, S., Grimaud, L., and Mazouffre, S., “Operation of a low-power Hall thruster: comparison between magnetically unshielded and shielded configuration,” *Plasma Sources Science and Technology*, Vol. 28, No. 3, mar 2019, pp. 034003.
- <sup>35</sup>Staack, D., Raitses, Y., and Fisch, N. J., “Temperature gradient in Hall thrusters,” *Applied Physics Letters*, Vol. 84, No. 16, apr 2004, pp. 3028–3030.
- <sup>36</sup>Adam, J. C., Héron, A., and Laval, G., “Study of stationary plasma thrusters using two-dimensional fully kinetic simulations,” *Physics of Plasmas*, Vol. 11, No. 1, 2004, pp. 295–305.
- <sup>37</sup>Janhunen, S., Smolyakov, A., Sydorenko, D., Jimenez, M., Kaganovich, I., and Raitses, Y., “Evolution of the electron cyclotron drift instability in two-dimensions,” *Physics of Plasmas*, Vol. 25, No. 8, aug 2018, pp. 082308.
- <sup>38</sup>Huang, M., Warner, K., Lehn, S., and Hieftje, G. M., “A simple approach to deriving an electron energy distribution from an incoherent Thomson scattering spectrum,” *Spectrochimica Acta Part B: Atomic Spectroscopy*, Vol. 55, No. 9, sep 2000, pp. 1397–1410.
- <sup>39</sup>Grimaud, L., Vaudolon, J., Mazouffre, S., and Boniface, C., “Design and characterization of a 200W Hall thruster in “magnetic shielding” configuration,” *52nd AIAA/SAE/ASEE Joint Propulsion Conference*, American Institute of Aeronautics and Astronautics, Reston, Virginia, jul 2016, pp. 1–17.
- <sup>40</sup>Raitses, Y., Smirnov, A., Staack, D., Keidar, M., and Fisch, N., “Characterization of plasma in a Hall thruster operated at high discharge voltage,” *41st AIAA/ASME/SAE/ASEE Joint Propulsion Conference & Exhibit*, No. July, American Institute of Aeronautics and Astronautics, Reston, Virginia, jul 2005, pp. 1–6.
- <sup>41</sup>Chaplin, V. H., Jorns, B. A., Lopez Ortega, A., Mikellides, I. G., Conversano, R. W., Lobbia, R. B., and Hofer, R. R., “Laser-induced fluorescence measurements of acceleration zone scaling in the 12.5 kW HERMeS Hall thruster,” *Journal of Applied Physics*, Vol. 124, No. 18, nov 2018, pp. 183302.

<sup>42</sup>Mazouffre, S., Grimaud, L., Tsikata, S., Matyash, K., and Schneider, R., “Rotating spoke instabilities in a wall-less Hall thruster: Experiments,” *Plasma Sources Science and Technology*, feb 2019.

<sup>43</sup>Matyash, K., Schneider, R., Mazouffre, S., Tsikata, S., and Grimaud, L., “Rotating spoke instabilities in a wall-less Hall thruster: simulations,” *Plasma Sources Science and Technology*, Vol. 28, No. 4, apr 2019, pp. 044002.